Electronic Supplementary Information

Electroreduction of CO$_2$ to CO over wide potential window by in situ electrodeposited CdCO$_3$/Cd-CP electrocatalysts

Jie Yang, Han Yang, Renjie Zhang, Guangying Zhou, Hongping Li* and Dexin Yang*

Green Catalysis Center, College of Chemistry, Zhengzhou University, Zhengzhou, Henan 450001, China.

E-mail: yangdx@zzu.edu.cn; lihongping@zzu.edu.cn

Experimental method

Materials. $Cd(NO_3)_2 \cdot 4H_2O$, Cd (<100 nm), and $CdCO_3$ were purchased from Aladdin Biochemical Technology Co., Ltd. Acetonitrile and ethanol were obtained from Comeo Chemical Reagent Co., Ltd. Concentrated sulfuric acid (95-98%) was supplied by Sinopharm Chem. Reagent Co., Ltd. Toray carbon paper (CP, TGP-H-60, 19 × 19 cm), Nafion D-521 dispersion (5% w/w in water and 1-propanol, ≥ 0.92 meg/g exchange capacity), and Nafion N-117 membrane (0.180 mm thick, ≥ 0.90 meg/g exchange capacity) were purchased from Alfa Aesar (China) Co., Ltd. Tetra-n-butylammonium hexafluorophosphate ($TBAPF_6$), 1-butyl-3-methylimidazolium hexafluorophosphate ([Bmim]PF_6, > 99%), 1-butyl-3-methylimidazolium tetrafluoroborate ([Bmim]BF_4, > 99%), 1-butyl-3-methylimidazolium bis (trifluoromethyl sulfonyl) imide ([Bmim]Tf_2N, > 99%), 1-butyl-3-methylimidazolium trifluoromethanesulfonate ([Bmim]OTf, > 99%), 1-ethyl-3-methylimidazolium hexafluorophosphate ([Emim]PF_6, > 99%), 1-butyl-3-methylimidazolium bromide ([Bmim]Br, > 99%), and 1-butyl-3-methylimidazolium chloride ([Bmim]Cl, > 99%) were obtained from the Centre of Green Chemistry and Catalysis, Lanzhou Institute of Chemical Physics, Chinese Academy of Sciences. N_2 (99.99%), CO_2 (99.999%), and N_2-diluted CO_2 gas with CO_2 concentrations of 10% (v/v) were provided by Henan Yumeng Technology Co., Ltd.

Physicochemical characterization. The microstructures of different electrocatalysts were characterized by Care Zeiss SIGMA 500 scanning electron microscope (SEM) and Tecnai G2 F20 transmission electron microscope (TEM) equipped with energy dispersive X-ray spectroscopy (EDX). The X-ray photoelectron spectroscopy (XPS) spectra were collected on the Thermo Scientific ESCALab 250Xi using a 200 W Al-Kα source. Typically, the binding energies obtained by the XPS analysis were corrected by referencing C 1s to 284.8 eV. X-Ray diffraction (XRD) analysis were performed for analyzing the crystalline lattice of various electrocatalysts on a X'Pert PRO X-ray diffractometer with Cu-Kα radiation (λ = 1.5406 Å) with the scan speed of 5°/min. The N_2 adsorption/desorption isotherms were conducted on a Micromeritics ASAP 2460 instrument at 77 K.

In situ electrochemical deposition of $CdCO_3$/Cd-CP-x electrocatalysts. The $CdCO_3$/Cd-CP-x electrocatalysts were prepared by an electrochemical deposition method. The electrolysis experiments were conducted in a commonly used H-type cell with three electrodes configuration, including a working electrode (CP, 1 cm × 1 cm),

a counter electrode (platinum gauzes), and a reference electrode. CO_2 saturated [Bmim]PF_6 (30 wt%)-acetonitrile-water (5 wt%) solution containing different concentrations of $Cd(NO_3)_2 \cdot 4H_2O$ of 0.5, 2, 3, 4, 6, 8 mmol L^{-1} and 0.5 M H_2SO_4 aqueous solution served as cathodic and anodic electrolytes, respectively. The electrolysis experiments were conducted at -2.0 V vs. Ag/Ag^+ maintained for 6 h at room temperature. After electrolysis, the cathodes were rinsed with ethanol for several times and dried in vacuum drying oven. Finally, the obtained cathodes were named $CdCO_3/Cd$-CP-x electrocatalysts, the x stands for the concentrations of $Cd(NO_3)_2 \cdot 4H_2O$.

The Cd-CP-2 electrocatalyst was prepared with the same method as $CdCO_3/Cd$-CP-2 electrocatalyst except that the CO_2 saturated electrolyte was replaced by N_2 saturated electrolyte.

The preparation of ex-situ electrocatalysts: Briefly, 3 mL acetone with 30 µL Nafion D-521 dispersion (5 wt%) was added into 50 mg Cd powders and 1 mg carbon black (Vulcan XC 72) and were ultrasonicated together for 30 min to form a homogeneous ink. After that, 0.303 mL ink containing about 5mg Cd catalyst was dripped onto the CP substrate (1×1 cm^2) and then dried in a vacuum oven under room temperature. The as-prepared CP electrode was the Cd/CP electrocatalyst. The $CdCO_3$/CP electrocatalyst was prepared with the same method except that the Cd powders was replaced by $CdCO_3$. The $CdCO_3$/Cd-(CP)-2 electrode was prepared with the same method except that the Cd powders was replaced by the $CdCO_3$/Cd sample which was scraped from $CdCO_3$/Cd-CP-2 electrocatalysts.

Electrochemical measurements. The electrochemical experiments were measured at 25 °C conducted in a commonly used H-type cell with three electrodes configuration, including a working electrode (CP, 1 cm × 1 cm), a counter electrode (platinum gauzes), and a reference electrode (Ag/Ag^+ with 0.01 M $AgNO_3$ in 0.1 M TBAP-acetonitrile). In the experiments, Nafion-117 proton exchange membrane was used to separate the cathode and anode compartments, which 30 mL 0.5 M H_2SO_4 aqueous solution and CO_2 saturated IL-acetonitrile solution served as anodic and cathodic electrolytes, respectively. Before starting the electrolysis experiment, the cathodic electrolytes were bubbled with pure CO_2 (or 10% CO_2, pure N_2) for 30 min under stirring to form gas-saturated electrolytes. Linear sweep voltammetric (LSV) measurements were carried out in gas-saturated electrolytes continuously purged with different gases at 20 sccm at

the potential range from −1.3 V to −2.5 V versus Ag/Ag$^+$ at a sweep rate of 20 mV s^{-1}. Slight magnetic stirring was employed to acquire uniform electrolytes.

Product analysis. During electrolysis, the gaseous products were collected and then analyzed by an Agilent 8860 gas chromatograph. The GC columns equipped with a thermal conductivity detector (TCD) to quantify hydrogen and a flame ionization detector (FID) to quantify carbon monoxide. After electrolysis, the liquid products were analyzed by ^{1}H nuclear magnetic resonance (^{1}H NMR) measured on a Bruker Avance III 600 HD spectrometer in deuterated dimethyl sulfoxide with TMS as internal standard. The Faradaic efficiency of the products was calculated according to the equation below through GC and NMR analysis.

Faradaic efficiency (FE) of CO, H_2 and HCOOH was calculated based on the following equation: FE = 2nF/Q, where 2 is the number of electrons required for these three products, n is the total amounts of products (moles), F represents Faraday constant (96485 C mol^{-1}), and the Q corresponds to the amount of cumulative charge during CO_2 electroreduction.

The CO production rate was determined by the production amounts of the CO per unit time (µmol h^{-1} cm^{-2}).

The CO_2 conversion rate for electroreduction CO_2 to CO was calculated by the equation as following[1].

CO_2 conversion rate (%) = (I_{CO}/2)·60·F·24300/V, where F is the Faraday constant; V is the volume of fed CO_2 in a minute (mL/min); (I_{CO}/2) means that two electrons are used to convert CO_2 to CO; 24300 (mL/mol) is the molar volume of CO_2 at 1 atm and 25 °C.

Tafel analysis. Tafel plots were constructed from partial current densities against overpotential. The partial current densities for CO at different potentials were calculated. The overpotential was obtained from the difference between the applied potential and the equilibrium potential obtained by extrapolation method.

Double-layer capacitance (C_{dl}) measurements. The electrochemical active surface area is proportional to C_{dl} value according to the previous reports.[2] C_{dl} was concluded in H-type electrolysis cell by measuring the capacitive current associated with double-layer charging according to the scan-rate dependence of cyclic voltammogram (CV). The CV measurements of the electrocatalysts were conducted from −1.6 to −1.8 V vs.

Ag/Ag$^+$ at various scan rates. The C_{dl} value was determined by plotting the Δj (j_a-j_c) at −1.7 V vs. Ag/Ag$^+$ against the square root of scan rates, in which the j_a and j_c were the anodic and cathodic current density, respectively.

Electrochemical impedance spectroscopy (EIS) study. The EIS measurements were performed in a single compartment cell with the amplitude of 5 mV from 10^{-2} to 10^5 Hz in 30 wt% [Bmim]PF$_6$/acetonitrile at an open circuit potential (OCP). The Zview software was used for fitting the data of the EIS measurements.

Computational Method. Density functional theory (DFT) calculations were performed using Vienna Ab initio Simulation Package (VASP)[3] with projector augment wave (PAW)[4] method and GGA-PBE[5] functional. The cutoff energy of 400 eV was used for both optimization and self-consistent calculation. The Cd(101) and CdCO$_3$(110) surface were represented by p(3×6×1) and p(2×2×1) supercell slab model with 4 formula atomic layers, where the top two formula layers were fully relaxed and the bottom two formula layers were fixed at the bulk lattice. CdCO$_3$/Cd was modeled by adding CdCO$_3$ cluster on Cd(101) surface, which enables to investigate the potential active sites on the interface and surface. Atomic positions are optimized with the convergence of energy and force less than 10^{-5} eV and 0.03 eV/Å, respectively. The Brillouin zone are sampled with 1×1×1, 2×2×1 and 1×1×1 Gamma-centered k-points for Cd(101), CdCO$_3$(110) and CdCO$_3$/Cd, respectively. DFT-D3[6] method was used to describe the dispersion correction. Computational hydrogen electrode (CHE) model[7] was used to calculated the free energy change of CO$_2$ reduction to CO reactions. ΔG were calculated by the following equation:

$$\Delta G = \Delta E + \Delta E_{ZPE} - T\Delta S + neU$$

Where ΔE, ΔE$_{ZPE}$, ΔS are the reaction energy from DFT calculation (Table S3), the correction of zero-point energy and the change of simulated entropy, respectively. T is the temperature and equals to 298 K. U and n are the applied potential and the number of transferred electrons, respectively.

Supplementary Figures
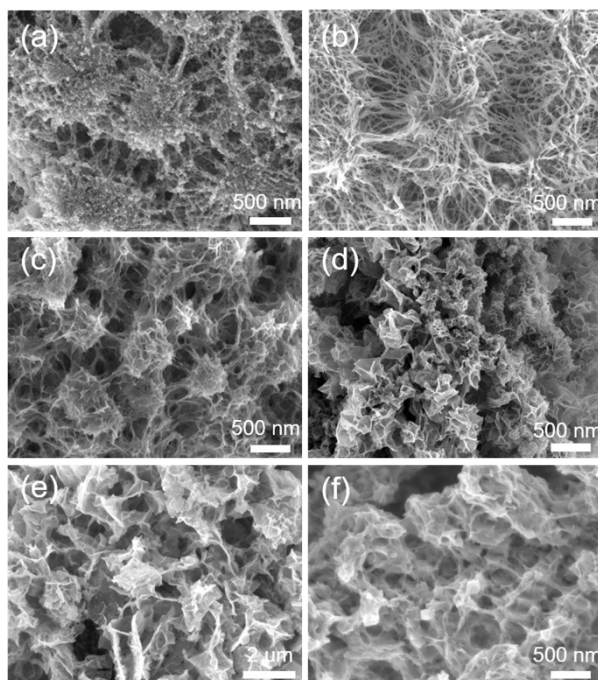
Fig. S1. The SEM images of (a-f) CdCO$_3$/Cd-CP-0.5, CdCO$_3$/Cd-CP-2, CdCO$_3$/Cd-CP-3, CdCO$_3$/Cd-CP-4, CdCO$_3$/Cd-CP-6, and CdCO$_3$/Cd-CP-8 electrocatalysts, respectively.

The detailed mechanism of CdCO$_3$/Cd nanostructures formation on the surface of CP substrate is shown in Eqs. S1-S6.[8, 9] In the cathodic process, Cd^{2+} ions can be directly reduced to produce Cd by accepting two electrons (Eq. S1). Due to the presence of NO$_3^-$ ions in the electrolyte, OH$^-$ ions would be formed on the CP surface through the reduction of NO$_3^-$ ions (Eq. S2). And then CO$_2$ molecules in the electrolyte near the CP surface can react with OH$^-$ ions to form CO$_3^{2-}$ ions (Eq. S3), which will interact with Cd^{2+} ions to generate CdCO$_3$ (Eq. S4). In addition, the OH$^-$ ions also can react with Cd^{2+} ions to produce Cd(OH)$_2$ (Eq. S5), while the Cd(OH)$_2$ can be reduced to Cd and OH$^-$ ions (Eq. S6). Therefore, the surface of CP substrate would in-situ form the CdCO$_3$/Cd nanostructures.

$$Cd^{2+} + 2e^- \rightarrow Cd \qquad\qquad\qquad (S1)$$

$$NO_3^- + H_2O + 2e^- \rightarrow NO_2^- + 2OH^- \qquad (S2)$$

$$CO_2 + OH^- \rightleftharpoons HCO_3^- \rightleftharpoons H^+ + CO_3^{2-} \quad (S3)$$

$$Cd^{2+} + CO_3^{2-} \rightarrow CdCO_3 \qquad (S4)$$

$$Cd^{2+} + 2OH^- \rightarrow Cd(OH)_2 \qquad (S5)$$

$$Cd(OH)_2 + 2e^- \rightarrow Cd + 2OH^- \qquad (S6)$$

$$Cd^{2+} + 2OH^- \rightarrow Cd(OH)_2 \qquad (S5)$$

$$Cd(OH)_2 + 2e^- \rightarrow Cd + 2OH^- \qquad (S6)$$
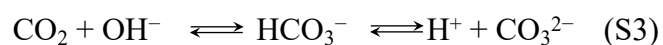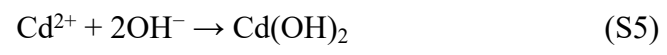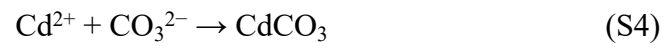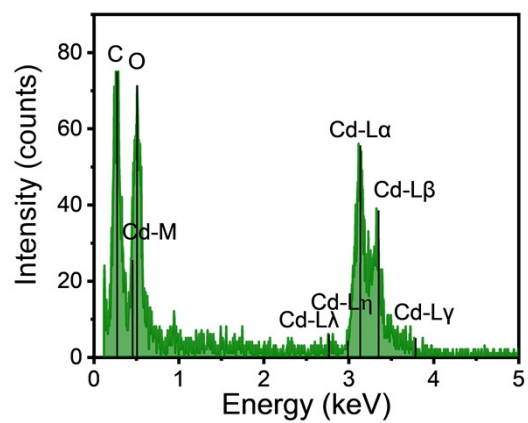
Fig. S2. EDX spectrum recorded of CdCO$_3$/Cd-CP-2 electrocatalyst.
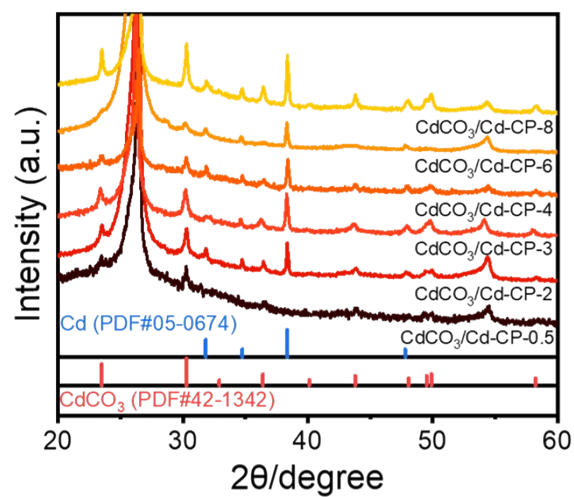
Fig. S3. The XRD spectra of CdCO$_3$/Cd-CP-x electrocatalysts.
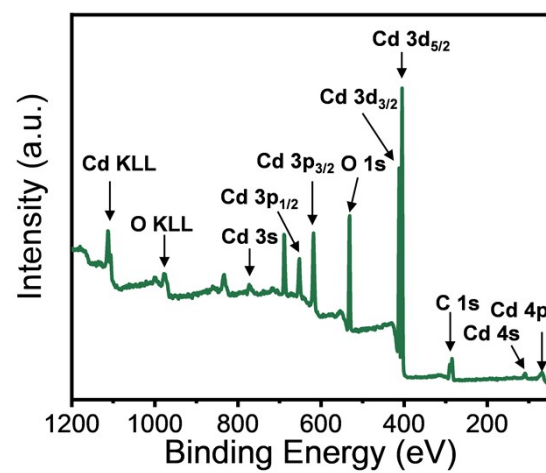
Fig. S4. The survey scan XPS spectrum recorded for $CdCO_3$/Cd-CP-2 electrocatalyst.
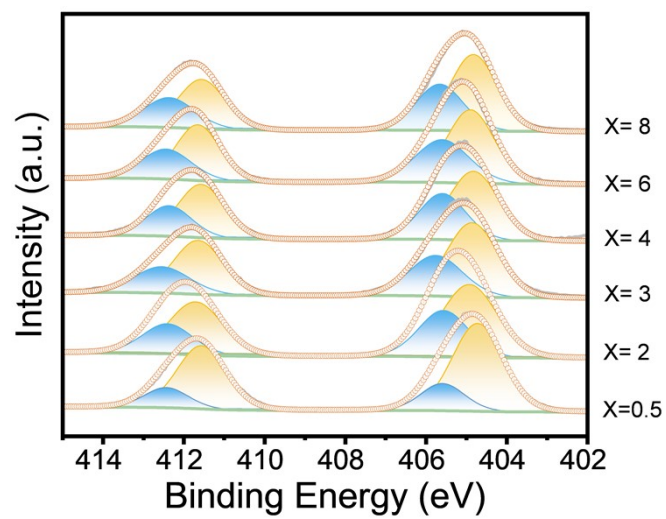
Fig. S5. The high resolution XPS spectra of Cd 3d of $CdCO_3$/Cd-CP-x electrocatalysts.
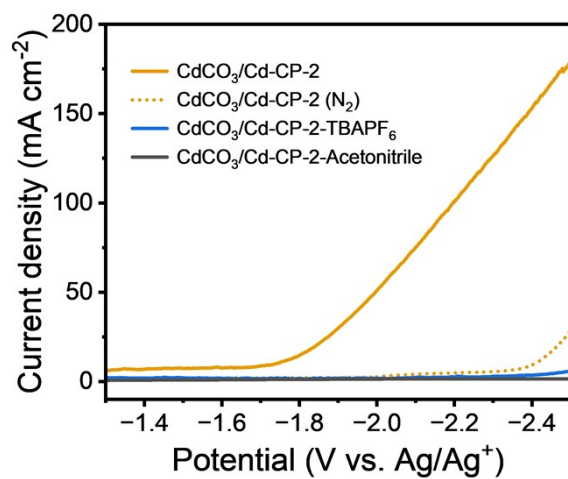
Fig. S6. LSV curves for different electrocatalysts in pure CO_2- or N_2- saturated electrolytes.
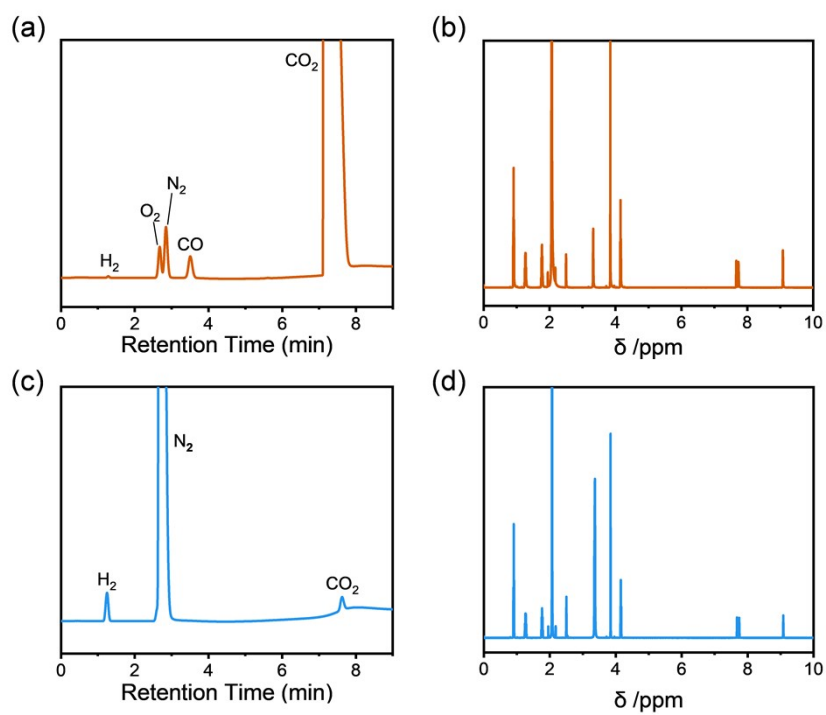
Fig. S7. GC spectra of gases product during electrolysis in (a) CO_2 and (c) N_2-saturated electrolyte. NMR spectra of electrolytes after electrolysis in (b) CO_2- and (d) N_2-saturated electrolyte.
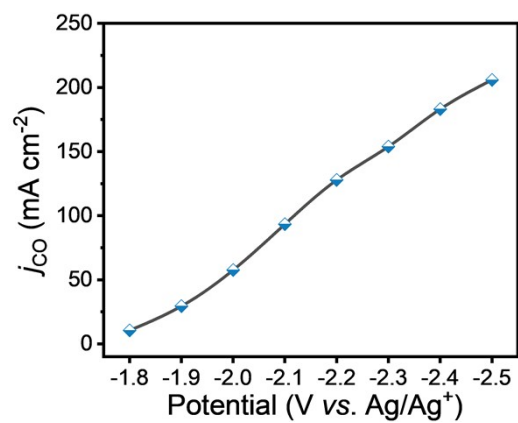
Fig. S8. Partial current density of CO over $CdCO_3$/Cd-CP-2 electrocatalyst in 30 wt% [Bmim]PF_6/acetonitrile electrolyte at different applied potentials.
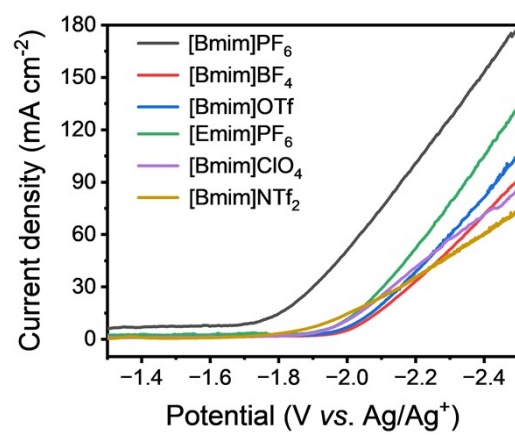
Fig. S9. LSV curves recorded in CO_2 saturated acetonitrile solution with 30 wt% different ILs.
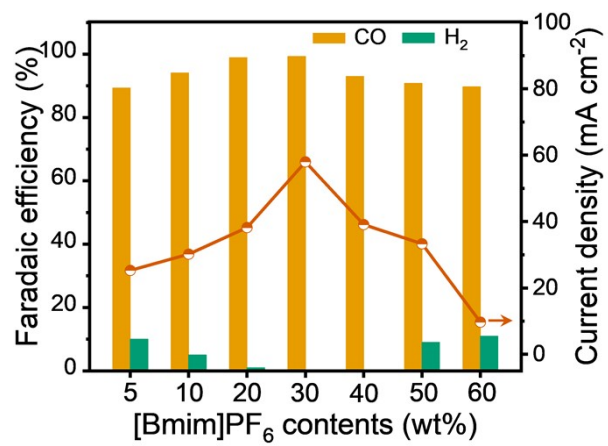
Fig. S10. CO FE and current density on CdCO$_3$/Cd-CP-2 electrocatalyst by changing the concentration of [Bmim]PF$_6$.
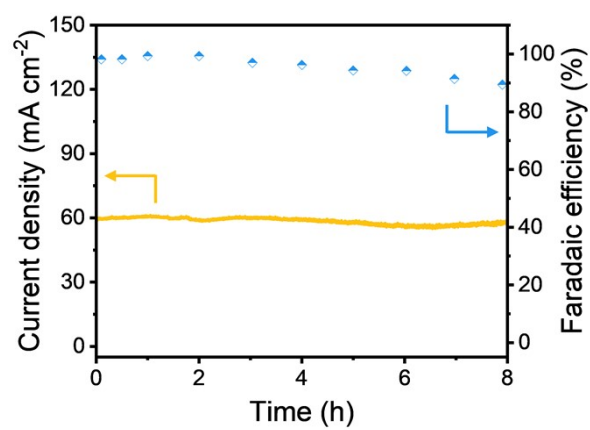
Fig. S11. The long-term stability of the CdCO$_3$/Cd-CP-2 electrode at the applied potential of −2.0 V vs. Ag/Ag$^+$.
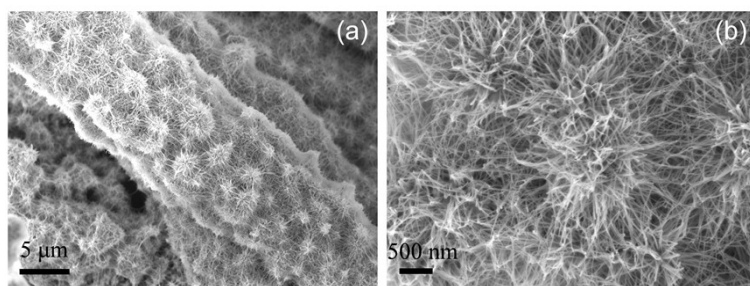
Fig. S12. The SEM (a) and enlarged SEM (b) images of CdCO$_3$/Cd-CP-2 after 8 h electrolysis.
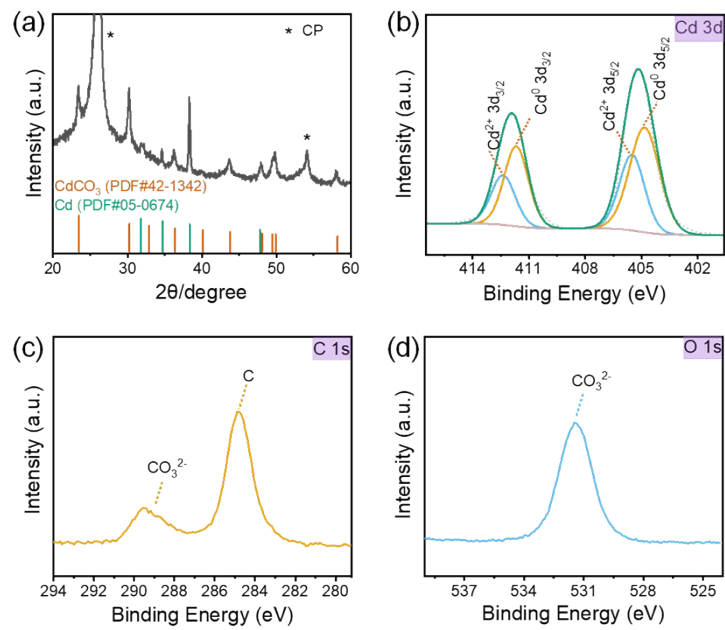
Fig. S13. The XRD (a) and XPS spectra of CdCO$_3$/Cd-CP-2 electrocatalyst after 8 h electrolysis: Cd 3d (b), C 1s (c) and O 1s (d).
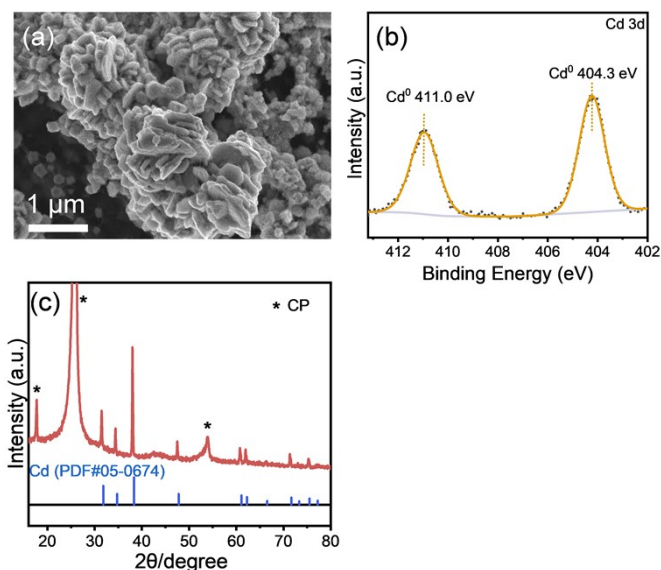
Fig. S14. The characterization of Cd-CP-2 electrocatalyst: (a) SEM image, (b) XPS spectrum of Cd 3d and (c) XRD spectrum.

Based on the results of Figs. S1 and S14, it can be concluded that the morphological change in $CdCO_3$/Cd-CP-x and Cd-CP-2 electrocatalysts may have two possible explanations. On the one hand, during the electrodeposition process, the morphology of the deposited materials ($CdCO_3$/Cd nanostructures) can affect by the $Cd(NO_3)_2 \cdot 4H_2O$ concentrations, which might dominate the nanostructure growth orientation and the crystal size.[10] The increase of $Cd(NO_3)_2 \cdot 4H_2O$ concentration can lead to a greater conductivity of the electrolyte that was caused by a higher quantity of ions present in the electrolyte, which may be associated with more $CdCO_3$/Cd nanocomposites formation on the CP substrate surface.[11, 12] Meanwhile, the shape and growth of the $CdCO_3$/Cd nanocomposites could be related to the rates of diffusion of Cd^{2+} ions and the generation of OH^- and CO_3^{2-} ions, which is also related to the $Cd(NO_3)_2 \cdot 4H_2O$ concentration.[11] On the other hand, the presence of CO_2 molecules in the electrolyte can serve as the precursor of $CdCO_3$ formation. In addition, the CO_2 molecules could regulate the morphology of the deposited material as a surface-controlling agent. CO_2 molecules in the electrolyte can be converted to some reduced intermediates of CO_2 electroreduction under negative potential, such as *OCHO intermediates.[13] These intermediates can adsorb on the deposited material surface to preferentially bind with certain specific surfaces, adjust the surface facet exposure, and thus change the morphology of the deposited material in synthesis process of the

21

electrocatalysts.[13, 14] Therefore, the nest-like morphology of $CdCO_3/Cd$-CP-2 electrocatalyst is obviously influenced by the $Cd(NO_3)_2 \cdot 4H_2O$ concentration and the presence of CO_2 molecules. However, a more detailed and precise mechanism for the relationship of the $CdCO_3/Cd$ nanocomposites morphological control, the $Cd(NO_3)_2 \cdot 4H_2O$ concentration, and the presence of CO_2 molecules merits closer investigation.
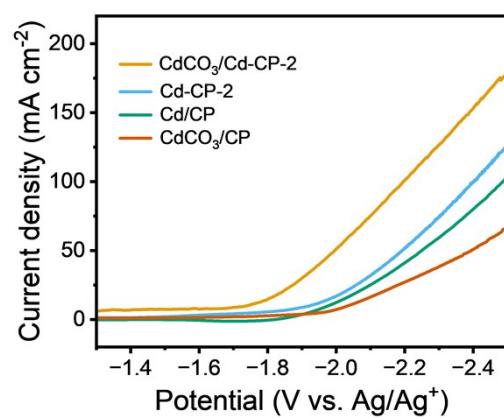
Fig. S15. LSV curves for different electrocatalysts in CO_2-saturated electrolytes.
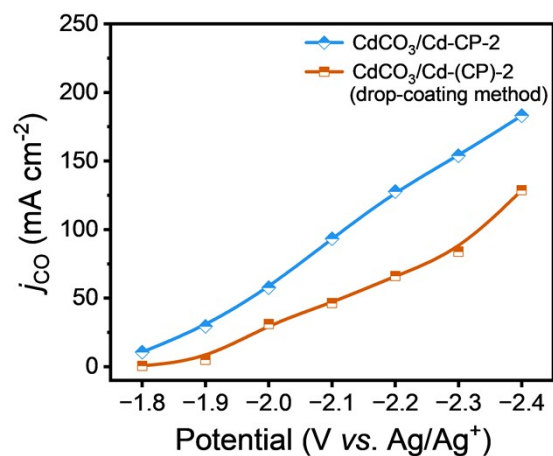
Fig. S16. The CO partial current densities over CdCO$_3$/Cd-CP-2 and CdCO$_3$/Cd-(CP)-2 electrode in 30 wt% [Bmim]PF$_6$/acetonitrile electrolyte at different applied potentials.
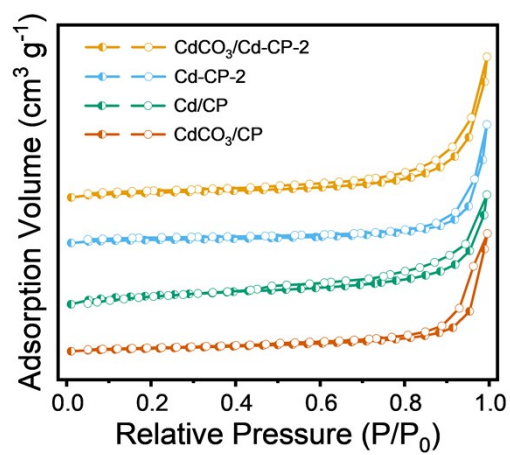
Fig. S17. The N$_2$ adsorption/desorption isotherms of CdCO$_3$/Cd-CP-2, Cd-CP-2, CdCO$_3$/CP and Cd/CP electrocatalysts.
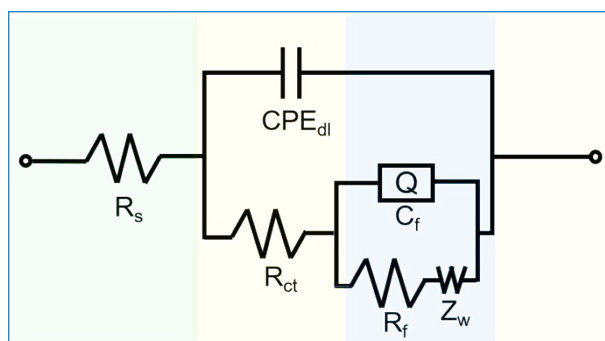
Fig. S18. Randles' equivalent circuit used for fitting the experimental impedance data of different electrodes: solution resistance (R_s), double layer capacitance (CPE_{dl}), electron transfer resistance (R_{ct}), film capacitance (C_f), film resistance (R_f) and Warburg-type impedance (Z_w).
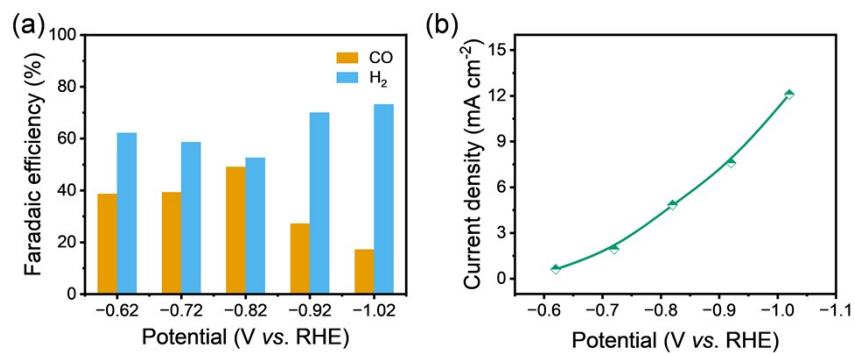
Fig. S19. CO FE and current density over CdCO$_3$/Cd-CP-2 electrocatalyst at different applied potentials in 0.5 M KHCO$_3$.
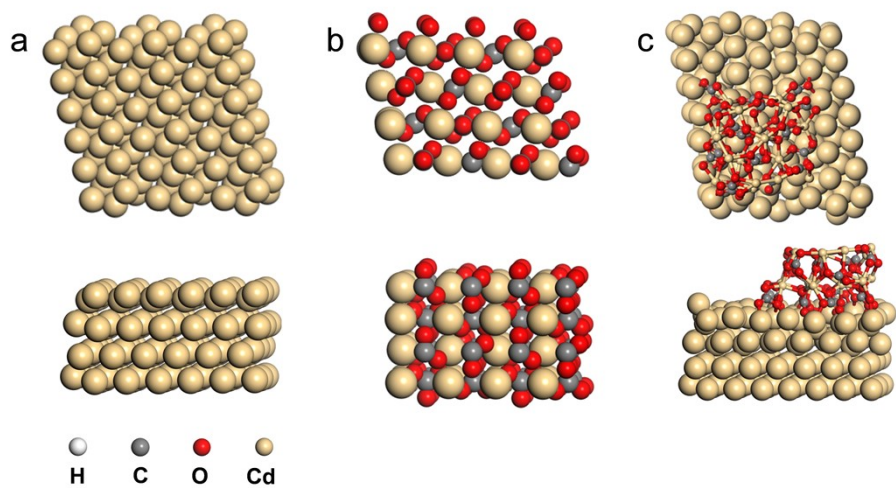
Fig. S20. The Cd(101), CdCO₃(110), and CdCO₃/Cd models after structural optimization.
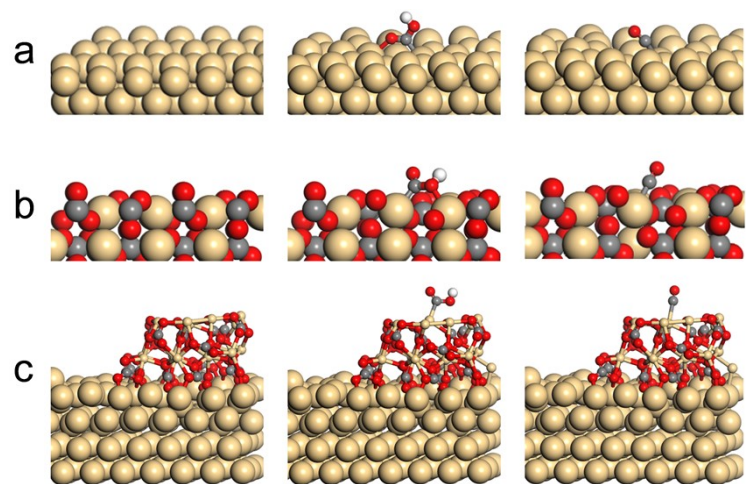
Fig. S21. The adsorption geometry of *COOH and *CO on (a) Cd(101), (b) CdCO₃(110), and (c) CdCO₃/Cd models.
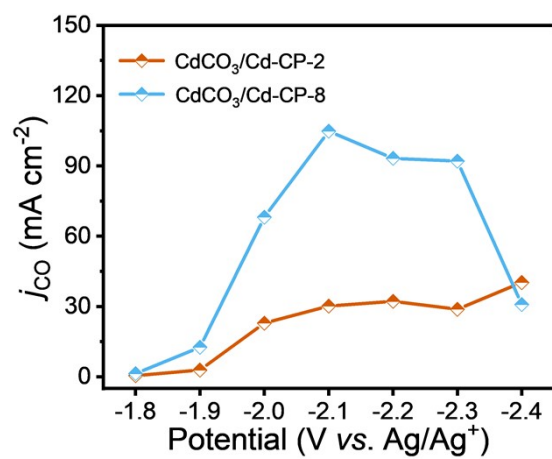
Fig. S22. Partial current density of CO on $CdCO_3$/Cd-CP-2 and $CdCO_3$/Cd-CP-8 electrocatalysts at different applied potentials under 10% CO_2.
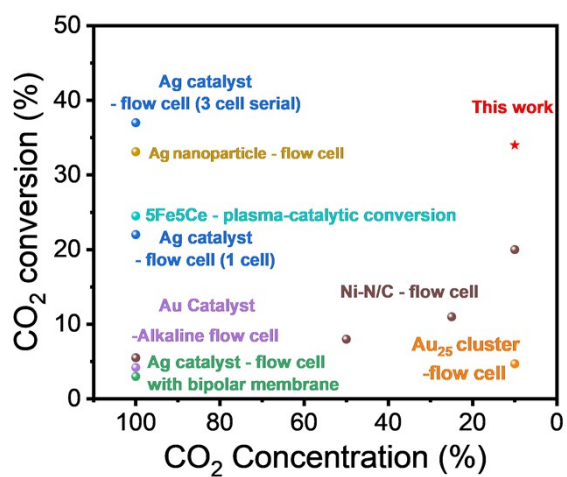
Fig. S23. The CO_2 conversion rate in different CO_2 concentration over different electrocatalysts[1, 15-20].

Supplementary Tables

Table S1. The atomic ratio of Cd and Cd^{2+} obtained from the Cd 3d XPS spectra of $CdCO_3$/Cd-CP-x electrocatalysts.

Electrocatalysts	Atomic ratio (Cd/Cd^{2+})
$CdCO_3$/Cd-CP-0.5	1:0.27
$CdCO_3$/Cd-CP-2	1:0.50
$CdCO_3$/Cd-CP-3	1:0.56
$CdCO_3$/Cd-CP-4	1:0.59
$CdCO_3$/Cd-CP-6	1:0.63
$CdCO_3$/Cd-CP-8	1:0.63

Table S2. EIS parameters, values of C_{dl} and Tafel slope, and the BET surface areas of different electrocatalysts.

Electrocatalysts	R_{ct} (Ω cm^2)	R_f (Ω cm^2)	C_{dl} (mF cm^{-2})	Tafel slope (mV dec^{-1})	BET surface area (m^2 g^{-1})
CdCO$_3$/Cd-CP-2	1.4	13.2	341.6	117	13.2
Cd-CP-2	1.9	38.2	270.4	158	6.38
Cd	5.1	290.8	146.9	160	1.02
CdCO$_3$	5.1	524.9	102.3	190	11.0

Table S3. The correction of zero-point energy and entropy effect of the adsorbed intermediates and molecules.

	ΔE_{ZPE} (eV)	$T\Delta S$ (eV)
*COOH	0.600	0.191
*CO	0.186	0.120
CO_2	0.311	0.661
CO	0.133	0.611

References

1.	Kim, B.; Seong, H.; Song, J. T.; Kwak, K.; Song, H.; Tan, Y. C.; Park, G.; Lee, D.; Oh, J. Over a 15.9% solar-to-CO conversion from dilute CO_2 streams catalyzed by gold nanoclusters exhibiting a high CO2 binding affinity. *ACS Energy Lett.* 2019, 5 (3), 749-757.

2.	Gao, S.; Lin, Y.; Jiao, X.; Sun, Y.; Luo, Q.; Zhang, W.; Li, D.; Yang, J.; Xie, Y. Partially oxidized atomic cobalt layers for carbon dioxide electroreduction to liquid fuel. *Nature* 2016, 529 (7584), 68-71.

3.	Kresse, G.; Furthmuller, J. Efficient iterative schemes for ab initio total-energy calculations using a plane-wave basis set. *Phys. Rev. B* **1996,** *54* (16), 11169.

4.	Blochl, P. E. Projector augmented-wave method. *Phys. Rev. B* **1994,** *50* (24), 17953-17979.

5.	Perdew, J. P.; Burke, K.; Ernzerhof, M. Generalized gradient approximation made simple. *Phys. Rev. Lett.* **1996,** *77* (18), 3865-3868.

6.	Grimme, S.; Antony, J.; Ehrlich, S.; Krieg, H. A consistent and accurate ab initio parametrization of density functional dispersion correction (DFT-D) for the 94 elements H-Pu. *J. Chem. Phys.* **2010,** *132* (15), 154104.

7.	Nørskov, J. K.; Rossmeisl, J.; Logadottir, A.; Lindqvist, L. Origin of the overpotential for oxygen reduction at a fuel-cell cathode. *J. Phys. Chem. B* **2004,** *108*, 17886-17892.

8.	Askarinejad, A.; Morsali, A., Synthesis of cadmium(II) hydroxide, cadmium(II) carbonate and cadmium(II) oxide nanoparticles; investigation of intermediate products. *Chem. Eng. J.* **2009**, *150* (2-3), 569-571.

9.	Wang, H.; Yang, D.; Yang, J.; Ma, X.; Li, H.; Dong, W.; Zhang, R.; Feng, C., Efficient Electroreduction of CO_2 to CO on Porous ZnO Nanosheets with Hydroxyl Groups in Ionic Liquid-based Electrolytes. *ChemCatChem* **2021**, *13* (11), 2570-2576.

10.	Chi, K.; Li, Q.; Meng, X.; Liu, L.; Yang, H., Morphology-controlled synthesis and characterization of CdTe micro-/nanoscale structures by electrodeposition method. *J. Mater. Sci.* **2017**, 52 (17), 10431-10438.

11.	Navarro-Gázquez, P. J.; Blasco-Tamarit, E.; Muñoz-Portero, M. J.; Solsona, B.; Fernández-Domene, R. M.; Sánchez-Tovar, R.; García-Antón, J., Influence of $Zn(NO_3)_2$ concentration during the ZnO electrodeposition on TiO_2 nanosponges used in photoelectrochemical applications. *Ceram. Int.* **2022**, 48 (10), 14460-14472.

12.	Sánchez-Tovar, R.; Blasco-Tamarit, E.; Fernández-Domene, R. M.; Villanueva-Pascual, M.; García-Antón, J., Electrochemical formation of novel TiO_2-ZnO hybrid nanostructures for photoelectrochemical water splitting applications. *Surf. Coat. Tech.* **2020**, 388, 125605.

13.	Wang, H.; Liang, Z.; Tang, M.; Chen, G.; Li, Y.; Chen, W.; Lin, D.; Zhang, Z.; Zhou, G.; Li, J.; Lu, Z.; Chan, K.; Tan, T.; Cui, Y., Self-Selective Catalyst Synthesis for CO_2 Reduction. *Joule* **2019**, 3 (8), 1927-1936.

14.	Qin, R.; Zheng, N., Catalysis Selects Its Own Favorite Facets. *Chem* **2019**, 5 (8), 1935-1937.

15.	Tan, X.; Yu, C.; Ren, Y.; Cui, S.; Li, W.; Qiu, J. Recent advances in innovative strategies for the CO_2 electroreduction reaction. *Energy Environ. Sci.* **2021,** *14* (2), 765-780.

16.	Ripatti, D. S.; Veltman, T. R.; Kanan, M. W. Carbon monoxide gas diffusion electrolysis that produces concentrated C_2 products with high single-pass conversion. *Joule* **2019,** *3* (1), 240-256.

17.	Salvatore, D. A.; Weekes, D. M.; He, J.; Dettelbach, K. E.; Li, Y. C.; Mallouk, T. E.; Berlinguette, C. P. Electrolysis of Gaseous CO_2 to CO in a Flow Cell with a Bipolar Membrane. *ACS Energy Lett.* **2017,** *3* (1), 149-154.

18.   Ashford, B.; Wang, Y.; Poh, C.-K.; Chen, L.; Tu, X. Plasma-catalytic conversion of CO_2 to CO over binary metal oxide catalysts at low temperatures. *Appl. Catal. B* **2020,** *276*, 119110.

19.   Endrodi, B.; Kecsenovity, E.; Samu, A.; Darvas, F.; Jones, R. V.; Torok, V.; Danyi, A.; Janaky, C. Multilayer electrolyzer stack converts carbon dioxide to gas products at high pressure with high efficiency. *ACS Energy Lett.* **2019,** *4* (7), 1770-1777.

20.   Kim, D.; Choi, W.; Lee, H. W.; Lee, S. Y.; Choi, Y.; Lee, D. K.; Kim, W.; Na, J.; Lee, U.; Hwang, Y. J.; Won, D. H. Electrocatalytic reduction of low concentrations of CO_2 gas in a membrane electrode assembly electrolyzer. *ACS Energy Lett.* **2021,** *6* (10), 3488-3495.